# Comparison of Different Virtual Inertia Control Methods for Inverter-based Generators

Dawei Sun, Hui Liu, Shunan Gao, Linlin Wu, Peng Song, and Xiaosheng Wang

***Abstract*—With the rapid development of inverter-based generators (IGs), power grid is faced with critical frequency stability challenges because the existing IGs have no inertia. To equip IGs with inertial response, researchers have proposed several virtual inertia control methods, which can be classified into two categories: virtual synchronous generator (VSG) control and droop control based on rate of change of frequency (ROCOF-droop control). In this paper, the comparison between both virtual inertia control methods is conducted from three perspectives: mathematical model, output characteristic and small-signal stability. State-space models are firstly built to analyze the control mechanism of VSG control and ROCOF-droop control methods. Simulation and eigenvalue analysis are conducted to study the transient responses and oscillation characteristics of both methods, which is helpful to understand the advantages and limitations of existing virtual inertia control methods. Finally, the obtained theoretical results are validated through real-time laboratory (RT-LAB) hardware-in-loop simulation platform.**

***Index Terms*—Virtual inertia control, virtual synchronous generator (VSG), small-signal model, stability analyses, subsynchronous oscillation.**

## I. Introduction

THE preservation of the environment has become the main motivation to integrate more inverter-based generators (IGs) in power system [1]. IGs are connected to the network by power electronic converter, which do not have any inertial response [2]. Therefore, replacing conventional sources with IGs will reduce the inertia of the whole power system. This fact is supported by [3], [4], both of which predicted that the increasing number of IGs in the UK could reduce the inertia constant by up to 70% between 2013 and 2033. Due to this inertia reduction, the rate of change of frequency (ROCOF) of the power system will be high enough to activate the load-shedding controller, even at a small magnitudes of load imbalance [5]. Therefore, several virtual inertia control methods were proposed for variable speed wind turbines and solar photovoltaic (PV) generators [6], [7].

Reference [8] originally proposed a method to provide virtual inertia based on the traditional grid-connected current control strategy for IGs. In this method, the virtual inertia was created by droop control based on ROCOF (ROCOF-droop control). However, IGs equipped with this control do not have grid-forming ability. Therefore, they are not able to work in stand-alone mode. To make IGs possess grid-forming ability, another control method, called virtual synchronous generator (VSG) [9], or virtual synchronous machine [10], or synchronous converter [11], was proposed for IGs to implement inertia response by emulating the swing equation of synchronous generators (SGs). To facilitate the explication, all methods with the idea of emulating swing equation are called VSG control in this paper. The swing equation, which is the essential element of VSG, is introduced in IGs to replace the original grid-connected current control. Therefore, the output voltage angle of IG is calculated by solving swing equation instead of phase lock loop (PLL).

On December 27, 2017, the first 100 MW renewable power station based on VSG technology in the world was completed in Hebei Province, China [14]. The completion of this project indicated that the virtual inertia control technology for IGs was applied to large-capacity, grid-connected renewable energy power stations. With the increase of grid-connected IGs equipped with virtual inertia, the analysis of the output characteristic and small-signal stability for these IGs has become vital to guarantee the safety of power grid. IGs with virtual inertia inherit the hardware structure of IG and emulate output characteristics of SGs. It is complicated to analyze the stability and inertial response of IGs. Existing relevant studies can be classified into two categories. On the one hand, the research was implemented for VSGs in microgrid. In [17], a VSG-based method with adaptive virtual inertia was proposed for PV generators in microgrid, which improved the frequency regulation ability of the grid. In [18], the effects of droop constant of primary frequency regulation and virtual inertia on the sub-synchronous and super synchronous oscillation modes were investigated in a microgrid system consisting of multiple PV-VSGs. On the oth-

Manuscript received: May 16, 2019; accepted: January 19, 2020. Date of CrossCheck: January 19, 2020. Date of online publication: June 9, 2020.

This work was supported by the technology project of State Grid Corporation of China and the technology project of State Grid Jibei Electric Power Corporation.



D. Sun (corresponding author), H. Liu, S. Gao, L. Wu, P. Song, and X. Wang are with State Grid Wind-Photovoltaic-Energy Storage Hybrid Power Generation Technology Laboratory, Beijing 100045, China, and they are also with State Grid Jibei Electric Power Research Institute (North China Electric Power Research Institute Co., Ltd.), Beijing 100045, China (e-mail: dddd129216713@126.com; Liu. hui. j@jibei. sgcc. com. cn; Gao. shunan@jibei. sgcc. com. cn; Wu. linlin@jiebi. sgcc. com. cn; Song. peng@jiebi. sgcc. com. cn; Wang. xiaosheng@jibei. sgcc.com.cn).

DOI: 10.35833/MPCE.2019.000330

er hand, the existing research concentrates on the virtual inertia control methods applied in grid-connected IGs. In [19], a VSG-based inertial response control method was investigated for wind turbines with variable speed. The proposed VSG method improved the inertial level and attenuated the ROCOF when a disturbance occured. In [20], the performance of virtual inertia control based on a case study of large-scale power grid was identified. The results indicated that IGs equipped with virtual inertia control may have negative effect on the damping of frequency stability, which is inconsistent with the conclusion of [19]. The main factors affecting the damping of grid-connected IGs with inertial response were identified in [21], whose results clarified that the effect of virtual inertia is negligible, while the primary frequency regulation droop coefficient is the key factor to decide the oscillation modal characteristics. However, [22] got the opposite result. In [22], the stability analysis proved that a small growth of virtual inertia may contribute serious negative damping in high-frequency oscillation modes, but the variation of frequency-droop coefficient has little influence on system stability.

Previous studies have provided inconsistent or even contradictory results. It is believed in some work [17]-[19] that virtual inertia of IGs offered improved damping for frequency or small-signal stability of electrical network. However, some other studies [20], [22] reported that the inertial response of IGs would contribute to negative damping for system stability on some occasions. Based on the above observations, it is worth noting that no prior research on this subject has given mechanism explanation for the contradictory conclusions. Furthermore, it is confusing how to use virtual inertia control in IGs because of the inconsistent characteristic stated by various literatures. To address this problem, the paper firstly investigates the existing virtual inertia control methods for IGs and classifies them into two categories: VSG control and ROCOF-droop control. The comparison between these two categories is conducted to comprehensively understand the characteristics of virtual inertia control method and clarify the opposite performance of virtual inertia control in different scenarios. Based on theoretical comparison between the two categories, the application scenarios of both controls are proposed to provide engineers with guidance to select the appropriate virtual inertia control for IGs.

The rest of this paper is organized as follows. The small-signal models of VSG control and ROCOF-droop control are established and compared in Section II. In Section III, the comparison of output characteristics between both methods is conducted to understand the inertia effect of IG on frequency stability. In Section IV, the stability of both methods is identified in various system scenarios and with different control parameters, which clarifies the application scenarios of VSG control and ROCOF-droop control. In Section V, theoretical results are verified with real-time laboratory (RT-LAB) and tested with a hardware-in-the-loop setup. Finally, brief conclusions are drawn in Section VI.

## II. Comparison Between Mathematic Models of VSG Control and ROCOF-droop Control Methods

An overview of the electrical system of studied grid-connected IG is shown in Fig. 1(a), where a typical IG is connected to the grid at the point of common coupling (PCC) through an LC filter, which is composed of the filter inductor $L_g$ and capacitor $C_g$. $R_l$ and $L_l$ denote the grid resistance and inductance at the PCC, respectively. The IG in Fig. 1(a) can be controlled by VSG control or ROCOF-droop control method. The control diagrams of both methods are respectively given by Fig. 1(b) and (c). The state-space models of these two virtual inertia control methods are built and compared in the following subsections. Moreover, the proposed models are verified by comparing its dynamic response to the time-domain simulation of a non-linear system model [16].

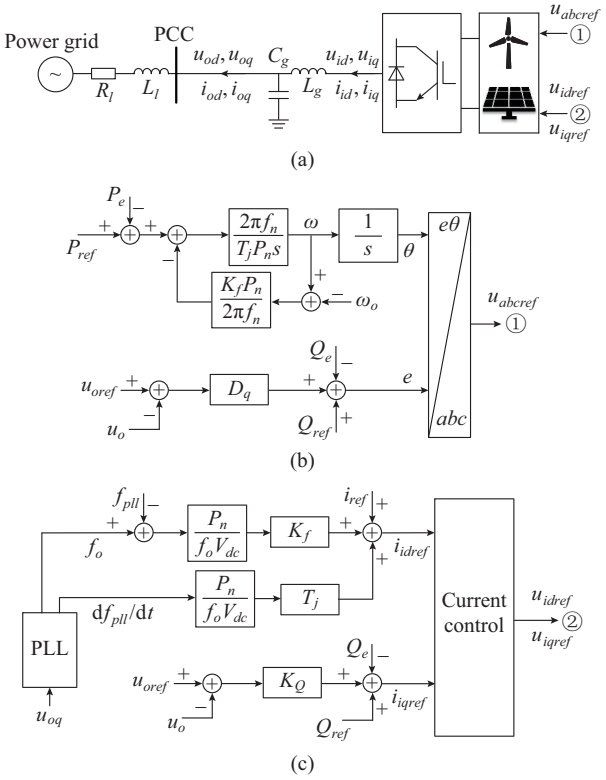


Fig. 1. Studied grid-connected IG system. (a) Overview of electrical system of studied grid-connected IG. (b) Control diagram of VSG control method. (c) Control diagram of ROCOF-droop control method.

### A. State-space Model of VSG Control

Based on Fig. 1(b), in VSG, the output active power $P_e$ is fed into the swing equation to calculate the angular frequency of the virtual rotor $\omega$, and the output reactive power $Q_e$ is fed into the voltage-droop control to calculate the amplitude of the voltage reference $e$. The state-space model of VSG control, whose diagram is shown in Fig. 1(b) is given by (1) and (2), where (1) reflects the inertia response and the primary frequency regulation and (2) embodies the voltage regulation.

$$\begin{cases} \dfrac{\mathrm{d}\omega}{\mathrm{d}t}=\dfrac{2\pi f_o}{T_j P_n}\left[P_{ref}-P_e-\dfrac{K_f P_n}{2\pi f_o}\left(\omega-\omega_o\right)\right] \\ \dfrac{\mathrm{d}\theta}{\mathrm{d}t}=\omega \end{cases} \tag{1}$$

$$e=Q_{ref}+D_q\left(u_{oref}-u_o\right)-Q_e \tag{2}$$

where $\theta$ is the phase angle of the voltage reference; $T_j$ is the virtual inertia constant; $P_n$ is the rated power of IG; $f_o$ is the nominal frequency (50 Hz); $\omega_o$ is the nominal angular frequency; $P_{ref}$ and $Q_{ref}$ are the set values of active and reactive power, respectively; $K_f$ is the droop coefficient of primary frequency regulation; $D_q$ is the voltage-droop control coefficient; $u_o$ is the root-mean-square (RMS) value of PCC voltage; and $u_{oref}$ is the set value of $u_o$.

### B. State-space Model of ROCOF-droop Control

The structures of PLL and current control in ROCOF-droop control are the same as the ones in traditional grid-connected current control for IGs [12]. State-space model of ROCOF-droop control, whose diagram is shown in Fig. 1(c), is given by (3)-(6), where (3) reflects the inertia response and primary frequency regulation, (4) embodies the *Q-V* droop mechanism, (5) introduces the dynamic characteristic of PLL, and (6) describes the state equations of current control. In (3)-(6), the three-phase voltage and current variables in stationary reference frame have been transformed into ones in synchronous reference frame (SRF), which is also known as *dq* frame. This transforming is achieved by amplitude-invariant Park transformation [15], which is given by (7).

$$i_{idref}=i_{ref}+\frac{P_n K_f}{V_{dc} f_o}\left(f_o-f_{pll}\right)+\frac{P_n T_j}{V_{dc} f_o}\frac{\mathrm{d}f_{pll}}{\mathrm{d}t} \tag{3}$$

$$i_{iqref}=Q_{ref}+K_Q\left(u_{odref}-u_{od}\right)-Q_e \tag{4}$$

$$\begin{cases} \dfrac{\mathrm{d}x_{pll}}{\mathrm{d}t}=-K_{Ipll}u_{oq} \\ \dfrac{\mathrm{d}\theta_{pll}}{\mathrm{d}t}=\omega_o-\left(x_{pll}-K_{Ppll}u_{oq}\right) \\ f_{pll}=\dfrac{1}{2\pi}\left[\omega_o-\left(x_{pll}-K_{Ppll}u_{oq}\right)\right] \\ \dfrac{\mathrm{d}f_{pll}}{\mathrm{d}t}=\dfrac{1}{2\pi}\left[0-\left(\dfrac{\mathrm{d}x_{pll}}{\mathrm{d}t}-K_{Ppll}\dfrac{\mathrm{d}u_{oq}}{\mathrm{d}t}\right)\right] \end{cases} \tag{5}$$

$$\begin{cases} \dfrac{\mathrm{d}u_{vd}}{\mathrm{d}t}=-K_{I1}\left(i_{idref}-i_{id}\right) \\ \dfrac{\mathrm{d}u_{vq}}{\mathrm{d}t}=-K_{I2}\left(i_{iqref}-i_{iq}\right) \\ u_{idref}=u_{vd}+K_{P1}\left(i_{idref}-i_{id}\right)-\omega_o L_g i_{iq} \\ u_{iqref}=u_{vq}+K_{P2}\left(i_{iqref}-i_{iq}\right)+\omega_o L_g i_{id} \end{cases} \tag{6}$$

$$\begin{bmatrix} x_d \\ x_q \end{bmatrix}=\frac{2}{3}\begin{bmatrix} \cos\left(\theta_{pll}\right) & \cos\left(\theta_{pll}-\dfrac{2\pi}{3}\right) & \cos\left(\theta_{pll}+\dfrac{2\pi}{3}\right) \\ -\sin\left(\theta_{pll}\right) & -\sin\left(\theta_{pll}-\dfrac{2\pi}{3}\right) & -\sin\left(\theta_{pll}+\dfrac{2\pi}{3}\right) \end{bmatrix}\begin{bmatrix} x_a \\ x_b \\ x_c \end{bmatrix} \tag{7}$$

where $x_a$, $x_b$, $x_c$ are the three-phase variables represented in stationary reference frame; subscripts $d$ and $q$ represent $d$-axis and $q$-axis components of three-phase variables in $dq$ frame, respectively; $i_{id}$ and $i_{iq}$ are the output currents of IG in $dq$ frame; $i_{idref}$ and $i_{iqref}$ are the set values of $i_{id}$ and $i_{iq}$, respectively; $i_{ref}$ is the initial set value of IG output current; $K_Q$ is the voltage-droop control coefficient in ROCOF-droop control; $V_{dc}$ is the direct-current voltage of inverter; $f_{pll}$ and $\mathrm{d}f_{pll}/\mathrm{d}t$ are the frequency and ROCOF obtained by PLL, respectively; $x_{pll}$ is the integrator state of the proportional-integral (PI) controller in PLL; $\theta_{pll}$ is voltage phase angle obtained by PLL; $K_{Ppll}$ and $K_{Ipll}$ are the proportional coefficient and integral coefficient in PLL, respectively; $u_{od}$ and $u_{oq}$ are the voltages of PCC in $dq$ frame; $u_{odref}$ is the set value of $u_{od}$; $u_{vd}$ and $u_{vq}$ are the integrator states of the PI controller in current control; and $K_{P1}$, $K_{P2}$, $K_{I1}$, and $K_{I2}$ are the proportional coefficients and integral coefficients in PI controller applied in current control, respectively.

### C. Comparative Analysis on Mathematical Models

The state-space models of VSG and ROCOF-droop control are analyzed and compared to study the difference between the two virtual inertia control methods from the following three perspectives.

*1) Stability Difference*

Based on (1), $\omega$ and $\theta$, which are the state variables reflecting swing characteristic of SGs, are introduced in VSG to achieve inertial response. Because both of the variables are not included in traditional IGs, the introduction of them will generate new oscillation mode, which makes IGs inherit the stability problem of rotor angle from SGs. On the other hand, the ROCOF-droop control equips IGs with inertial response without introduction of new state variable, which indicates that no new oscillation mode will be produced. However, in this method, derivative controller is applied in PLL to capture the ROCOF for emulating inertia, which will amplify high-frequency noise and may stimulate vibration.

*2) Difference in Power Control*

From the VSG control diagram in Fig. 1(b), the swing equation is emulated in VSG to equip IGs with power-angle characteristic of SGs. Therefore, the output power of VSG is determined by controlling the reference phase angle of voltage. However, through the method of ROCOF-droop control, the output power of IG is regulated by setting reference current, which is calculated from droop control according to the frequency and ROCOF obtained by PLL.

*3) Difference in Primary Frequency Regulation*

By comparing the swing equations of VSG and SG, it indicates that the primary frequency regulation mechanism of VSG is similar to that of SG. The reference signal of primary frequency regulation power is calculated by multiplying the difference between the angular frequency of rotor and the nominal angular frequency with a droop coefficient. The reference signal will be transferred through an integral controller with time constant $T_j$ to influence the rotor angular frequency, which will further change the reference phase angle of voltage and implement primary frequency regulation. However, in droop control, the reference signal for primary

frequency regulation is generated to directly control the output current of IG for the purpose of frequency regulation, which makes IG with droop control output the power of primary frequency regulation more quickly than VSG.

The above analysis will be verified by simulations, small-signal model and RT-LAB hardware-in-loop experiments.

### *D. Small-signal Model*

The non-linear state-space models of VSG control and ROCOF-droop control methods are listed in (1), (2) and (3)-(6), respectively. By combining them with the state equations of other parts in Fig. 1 (refer to [20]), the state-space models of grid-connected IG systems equipped with VSG control and ROCOF-droop control can be established. The corresponding linearized small-signal models of the systems based on VSG control and ROCOF-droop control can be found from the state-space models and defined on the general form given by (8) and (9).

$$\Delta\dot{\boldsymbol{x}}_1 = \boldsymbol{A}_1\Delta\boldsymbol{x}_1 \tag{8}$$

$$\Delta\dot{\boldsymbol{x}}_2 = \boldsymbol{A}_2\Delta\boldsymbol{x}_2 \tag{9}$$

where $\Delta\boldsymbol{x}_1 = [\Delta i_{id}, \Delta i_{iq}, \Delta u_{od}, \Delta u_{oq}, \Delta i_{od}, \Delta i_{oq}, \Delta\omega, \Delta\theta]^{\mathrm{T}}$, $i_{od}$ and $i_{oq}$ are the input currents from IG to PCC in $dq$ frame; $\Delta\boldsymbol{x}_2 = [\Delta i_{id}, \Delta i_{iq}, \Delta u_{od}, \Delta u_{oq}, \Delta i_{od}, \Delta i_{oq}, \Delta x_{pll}, \Delta\theta_{pll}, \Delta u_{vd}, \Delta u_{vq}]^{\mathrm{T}}$; and the elements in $\boldsymbol{A}_1$ and $\boldsymbol{A}_2$ matrices are given in Appendix A.

The model defined by (8) and (9) expresses the characteristic under small-signal deviations around the point of linearization.

### *E. Model Validation*

Through (8) and (9), it is possible to calculate step responses of output power of IG ($P_{out}$) caused by a "1.0 p.u.→ 1.1 p.u." change in reference power. The theoretical results are shown in Fig. 2 along with the corresponding simulation results obtained by MATLAB. Parameters used for both theoretical calculation and simulation are the same, as listed in Table I.

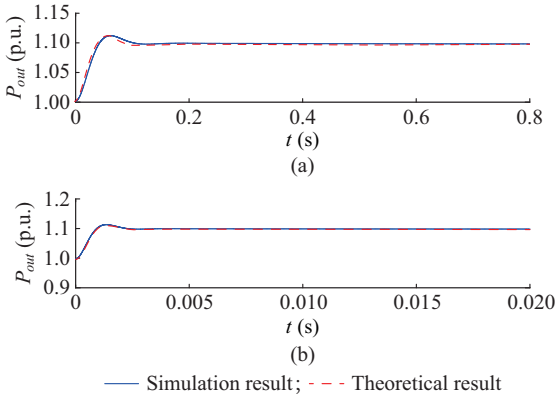


Fig. 2. Comparisons of responses obtained with both models. (a) Validation for small-signal model of VSG. (b) Validation for small-signal model of ROCOF-droop control.

As it is demonstrated in Fig. 2, for VSG control and ROCOF-droop control, the simulation results almost overlap the corresponding theoretical results. Thus, it can be concluded that the effectiveness of small-signal models are verified. The comparison in response speed of $P_{out}$ between Fig. 2(a) and (b) reflects that IG with ROCOF-droop control regulates $P_{out}$ faster than VSG control, which verifies the theoretical analysis results in Section II-C.

TABLE I
PARAMETERS OF STUDIED SYSTEM

| Parameter | Value | Parameter | Value | Parameter | Value |
|---|---|---|---|---|---|
| $P_{ref}$ | 500 kW | $Q_{ref}$ | 0 kvar | $K_{P1}$, $K_{P2}$ | 5 |
| $C_g$ | 300 μF | $T_j$ | 0.1 s | $K_{I1}$, $K_{I2}$ | 2 |
| $L_g$ | 150 μH | $K_f$ | 20 | $R_l$ | 1.264 mΩ |
| $D_q$ | 2000 | $K_Q$ | 4 | $L_l$ | 0.0386 mH |

## III. COMPARISON IN TRANSIENT OUTPUT CHARACTERISTICS BETWEEN VSG CONTROL AND ROCOF-DROOP CONTROL METHODS

The transient characteristics of output power in IGs equipped with VSG control and ROCOF-droop control are studied based on the simulation system shown in Fig. 3, where the base capacity $S_B$ is 500 MVA and base voltage $V_B$ is 110 kV. In the simulation, two loads ($L_1$ and $L_2$) are powered by a generator $SG_1$ and another generator ($SG_2$, VSG IG or ROCOF-droop IG). At 12 s, $L_3$ is connected into the system. At 40 s, the droop coefficients of primary frequency regulation ($K_f$) of different generators are changed. The following three scenarios are studied: ① scenario 1, only close $S_1$ to connect $SG_2$; ② scenario 2, only close $S_2$ to connect VSG IG; ③ scenario 3, only close $S_3$ to connect ROCOF-droop IG. The parameters of applied generators are listed in Table II.

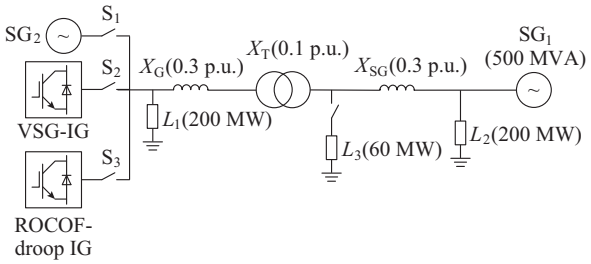


Fig. 3. Simulation system for comparing generators.

TABLE II
PARAMETERS OF STUDIED GENERATORS

| Generator | Capacity (MVA) | Electrical distance to $L_3$ (p.u.) | $T_j$ (s) | $K_f$ (change at 40 s) |
|---|---|---|---|---|
| $SG_1$ | 500 | 0.3 | 3.20 | 20→10 |
| $SG_2$ | 500 | 0.4 | 6.40 | 20→30 |
| VSG IG | 500 | 0.4 | 6.40 | 20→30 |
| ROCOF-droop IG | 500 | 0.4 | 0.64 | 20→30 |

In scenario 1, the outputs of $SG_1$ and $SG_2$ are shown in Fig. 4. Based on the law of energy conservation, when a power impact ($L_3$) occurs in the network, the power impact

will be "shared" by various generators. Figure 4 shows the sharing rule of power impact between different SGs, which is summarized as the "three-stage principle" in [23].

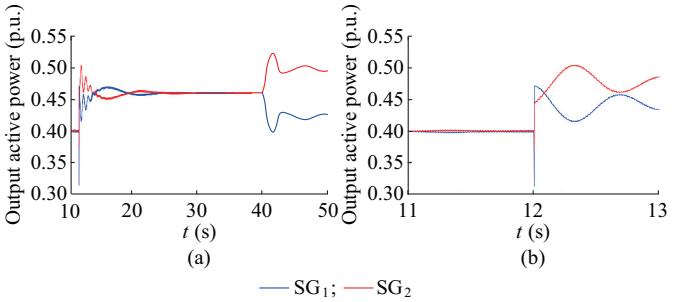


Fig. 4. Distribution of $L_3$ between $SG_1$ and $SG_2$. (a) Overall situation. (b) $L_3$ is connected.

Stage 1: at the instant immediately following the impact ($L_3$ is connected in system), the SG electrically close to the impact will pick up the greater share of the load and the energy source of power supplied by the generators is the energy stored in their magnetic fields. According to Fig. 4(b), at 12 s, $SG_1$, which is electrically closer to $L_3$ than $SG_2$, outputs more power to supply $L_3$ compared with $SG_2$.

Stage 2: before the governor action begins, various SGs will share the load increase based on their inertia constants. In Fig. 4(b), during 12-13 s, $SG_2$, which has larger $T_j$, outputs more power to supply $L_3$ compared with $SG_1$.

Stage 3: after governor action fully functions, different SGs will share the load impact based on their droop coefficients of primary frequency regulation. In Fig. 4(a), during 30-40 s, $SG_1$ and $SG_2$ pick up the same share of the impact $L_3$ because they have the same $K_f$. At 50 s, $SG_1$ and $SG_2$ respectively pick up 25% and 75% of $L_3$ because of the new value of $K_f$ after 40 s.

### A. Transient Output Response of VSG IG

In scenario 2, the simulation results of $SG_1$ and VSG IG output are shown in Fig. 5.

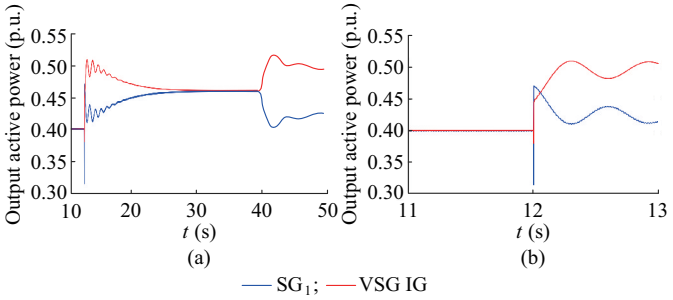


Fig. 5. Distribution of $L_3$ between $SG_1$ and VSG IG. (a) Overall situation. (b) $L_3$ is connected.

As shown in Fig. 5, the sharing rule of $L_3$ between SG1 and VSG IG accords with the "three-stage principle" in [23]. At the instant immediately following the impact, $SG_1$, which is electrically closer to $L_3$, picks up greater share of the load than that of VSG IG. Before the governor action begins, VSG IG, which equips with larger $T_j$, outputs more power to supply $L_3$ than $SG_1$. After governor action fully functions (30-40 s), $SG_1$ and VSG IG take the same share of the $L_3$ as they have the same $K_f$. Then, $SG_1$ and VSG IG respectively pick up 25% and 75% of $L_3$ at the end of the simulation because the two generators have different $K_f$ values after 40 s.

By comparing the results in Figs. 4 and 5, the principle of VSG IG to pick up the share of power impact is the same as that of SGs, which indicates that VSG IG inherits the response characteristic of transient output of SG.

### B. Transient Output Response of ROCOF-droop IG

In scenario 3, the simulation results of $SG_1$ and ROCOF-droop IG output are shown in Fig. 6. As shown in Fig. 6, the sharing principle of power impact between $SG_1$ and ROCOF-droop IG is not in accordance with the "three-stage principle". In Fig. 6(b), at the instant immediately following the impact, ROCOF-droop IG picks up no share of $L_3$. Based on the analysis in Section II-C, the above phenomenon can be explained as follows: the outputs of ROCOF-droop IG are regulated by setting reference current, which is calculated based on the frequency and ROCOF obtained by PLL. When $L_3$ is connected, the system frequency cannot change instantly. Therefore, the reference current remains unchanged and no variation appears in the output of ROCOF-droop IG.

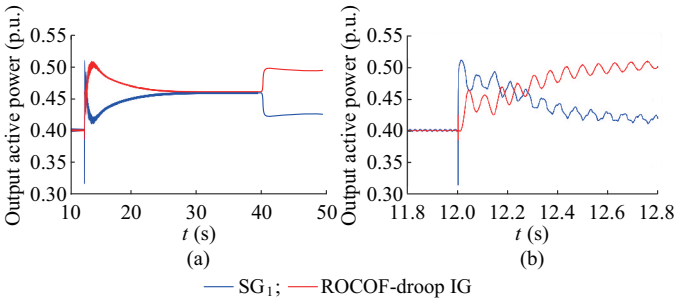


Fig. 6. Distribution of $L_3$ between $SG_1$ and ROCOF-droop IG. (a) Overall situation. (b) $L_3$ is connected.

Based on the output of $SG_1$ and ROCOF-droop IG during 12-30 s in Fig. 6(a), before governor action begins, ROCOF-droop IG, which equips with smaller $T_j$ ($T_j$ = 0.64 s), outputs more power than that of $SG_1$. It indicates that $SG_1$ and ROCOF-droop IG do not share the power impact based on their inertia constants.

By comparing the results of Figs. 4 and 6, the principle of ROCOF-droop IG to pick up the share of power impact is different from that of SGs before governor action begins.

## IV. Comparison in Small-signal Stability Between VSG Control and ROCOF-droop Control Methods

### A. System Eigenvalue Analysis

Based on the proven small-signal model of IGs based on VSG control and ROCOF-droop control, the eigenvalues of $\boldsymbol{A}_1$ and $\boldsymbol{A}_2$ matrices in (8), (9) can be calculated to systematically analyze the oscillation modes of VSG IG and ROCOF-

droop IG. State variables which are strongly correlated with the oscillation modes can be identified by the combination of right and left eigenvectors [10]. All the oscillation results based on eigenvalue analysis are listed in Tables III and IV.

TABLE III
OSCILLATION MODES FOR VSG IG

| Mode | Eigenvalue | Damping ratio | Oscillation frequency (Hz) | State variable of strong correlation |
|---|---|---|---|---|
| 1 | $\lambda_1$, $\lambda_2$ | 0.0015 | 1222.00 | $u_{od}$, $u_{oq}$, $i_{od}$, $i_{oq}$ |
| 2 | $\lambda_3$, $\lambda_4$ | 0.0035 | 1123.00 | $u_{od}$, $u_{oq}$, $i_{od}$, $i_{oq}$ |
| 3 | $\lambda_5$, $\lambda_6$ | 1.0000 | 0.48 | $\omega$, $\theta$, $P_e$ |
| 4 | $\lambda_7$, $\lambda_8$ | 0.3700 | 7.98 | $\omega$, $\theta$, $P_e$ |

TABLE IV
OSCILLATION MODES FOR ROCOF-DROOP IG

| Mode | Eigenvalue | Damping ratio | Oscillation frequency (Hz) | State variable of strong correlation |
|---|---|---|---|---|
| 1 | $\lambda_1$, $\lambda_2$ | 0.00032 | 3425.00 | $u_{od}$, $u_{oq}$, $i_{od}$, $i_{oq}$ |
| 2 | $\lambda_3$, $\lambda_4$ | 0.00140 | 3325.00 | $u_{od}$, $u_{oq}$, $i_{od}$, $i_{oq}$ |
| 3 | $\lambda_5$, $\lambda_6$ | 0.64000 | 317.00 | $i_{id}$, $i_{iq}$ |
| 4 | $\lambda_7$, $\lambda_8$ | 1.00000 | 0 | $u_{vd}$, $u_{vq}$ |
| 5 | $\lambda_9$, $\lambda_{10}$ | 0.10000 | 3.37 | $x_{pll}$, $\theta_{pll}$ |

*1) Difference in Oscillation Mode Between VSG IG and ROCOF-droop IG*

Based on Table III, in VSG IG, the oscillation modes 1 and 2 are strongly correlated with the state variables generated by filter, which indicates that the damping ratios of high-frequency oscillation modes 1 and 2 are mainly dependent on the parameter of a filter. The damping characteristic of oscillation modes 3 and 4 is highly sensitive to the parameter of inner-loop control of IG. And the damping ratio of oscillation mode 5 is decided by PLL parameter. The above oscillation feature of ROCOF-droop IG is the same as the IG with traditional grid-connected current control [17]. By comparing the traditional IG control strategy, the application of ROCOF-droop control does not introduce any new oscillation mode. On the other hand, based on Table III, due to the emulation of swing equation, oscillation modes 3 and 4 of VSG IG, which do not exist in the traditional IG, are introduced by the application of VSG control. Meanwhile, because VSG IG has no inner-loop control and PLL, no corresponding oscillation mode exists in VSG IG.

*2) Influence of PLL*

Because VSG IG has grid-forming ability and can operate in stand-alone mode [14], PLL is not needed in VSG IG. However, PLL is significant in ROCOF-droop IG because it is used to synchronize the inverter to the grid and calculate the predefined output current of IG. The result of Table IV clarifies that oscillation mode 5 of ROCOF-droop IG is highly sensitive to the parameter of PLL. Therefore, PLL has an important influence on not only the output response but also the stability of ROCOF-droop IG.

*3) Common Oscillation Mode*

The characteristic of oscillation modes 1 and 2 of VSG IG is similar to that of ROCOF-droop IG. The high-frequency oscillation modes in both IGs are of small damping ratio and are relevant with the filter of IG. This high-frequency oscillation mode caused by LC resonance between LC filter and transmission line exists in any grid-connected IG system with a filter, no matter which control strategy is applied.

## B. Impact of Control Parameters on Stability

In both of VSG IG and ROCOF-droop IG, the $K_f$ and $T_j$ are two significant parameters to decide the ability of IG to actively take part in the power regulation of the grid. The impact imposed by these two parameters on the stability are introduced as follows.

*1) Impact of $K_f$*

The eigenvalue trajectories of both kinds of IGs with $K_f$ changing from 20 to 5 are given by Fig. 7. From Fig. 7(a), it is observed that $\lambda_7$ and $\lambda_8$ monotonously move toward right when $K_f$ increases, which indicates that the damping of oscillation mode corresponding to $\lambda_7$ and $\lambda_8$ decreases rapidly when $K_f$ increases. When $K_f$ is smaller than 6.75, VSG IG will produce negative damping that is sufficient to cause unstable oscillation. However, in ROCOF-droop IG, eigenvalues are insensitive to the change of $K_f$, which implies that the stability of ROCOF-droop IG is not influenced by $K_f$.

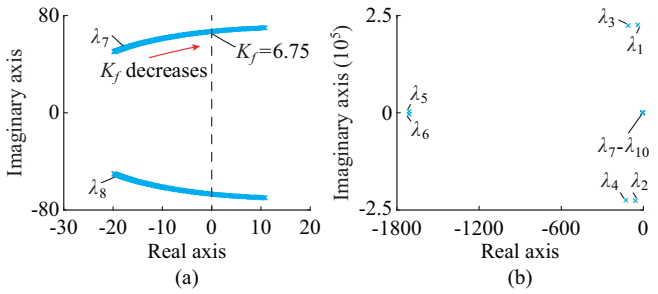


Fig. 7. Impact of $K_f$ on eigenvalues.

$K_f$ is not only a key parameter affecting the stability, but also an important indicator for determining the capability of primary frequency regulation of IGs. IGs equipped with larger $K_f$ will output more active power when frequency drops. By considering both the stability and the capability of primary frequency regulation, the value of $K_f$ in VSG IG or ROCOF-droop IG should be set as the maximum value given by the standard range.

From the perspective of energy for primary frequency regulation, no matter for VSG IG or ROCOF-droop IG, a greater $K_f$ requires IGs to save more reserved power or install more battery for energy storage, which has a negative effect on the economic benefit for IG owners.

*2) Impact of $T_j$*

The eigenvalue trajectories of VSG IG and ROCOF-droop IG when sweeping $T_j$ from 0.01 s to 20 s are shown in Fig. 8. Figure 8 shows that, in VSG IG, $\lambda_7$ and $\lambda_8$ move toward right when $T_j$ increases. The similar trend appears for $\lambda_1$ and $\lambda_2$ in ROCOF-droop IG. Based on the results of Fig. 8, unsta-

ble oscillation will appear in VSG IG when $T_j$ is larger than 9. And the marginal value of $T_j$ in ROCOF-droop IG is 0.7. Comparing with ROCOF-droop control, the application of VSG control is able to enlarge the value range of $T_j$.

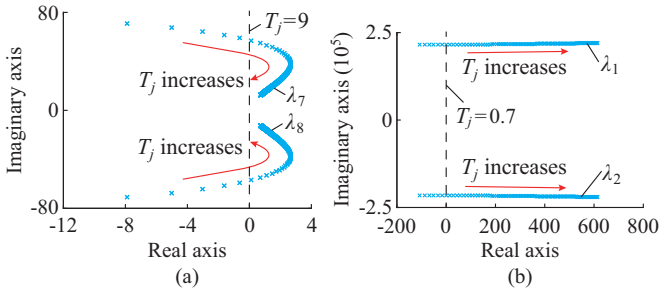


Fig. 8. Impact of $T_j$ on eigenvalues. (a) VSG IG. (b) ROCOF-droop IG.

Similar to $K_f$, $T_j$ is a key parameter for both the stability and the capability of frequency regulation. A larger $T_j$ implies a bigger inertia for IGs. The comparison between Fig. 8(a) and (b) indicates that VSG IG can equip with a bigger $T_j$ and a larger inertia. However, in ROCOF-droop IG, $T_j$ could not be set as large as the value in VSG IG because of the unstable high-frequency oscillation.

### C. Adaptation of VSG IG and ROCOF-droop IG Under Various Grid Conditions

For systematically analyzing the adaptation of VSG IG and ROCOF-droop IG, the damping characteristics of both IGs are investigated under various conditions, for instance, different grid impedances and voltage levels.

#### 1) Impact of Grid Impedance on Stability

The grid impedance $Z_l$ is defined as:

$$Z_l = \frac{S_b}{V_b^2}\sqrt{R_l^2 + \left(100\pi L_l\right)^2} \tag{10}$$

where $S_b$ = 500 kVA and $V_b$ = 315 V are the rated power and voltage of IG, respectively.

The eigenvalue trajectories of VSG system when sweeping $Z_l$ from 0.01 p.u. to 6 p.u. are shown in Fig. 9.

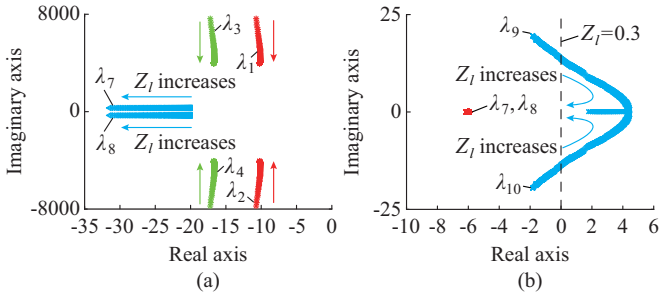


Fig. 9. Impact of $Z_l$ on eigenvalues. (a) VSG IG. (b) ROCOF-droop IG.

As shown in Fig. 9(a), all eigenvalues stay in the left half plane as $Z_l$ changing from 0.01 p.u. to 1 p.u., which indicates that the damping of VSG IG is positive. Figure 9(b) indicates that, in ROCOF-droop IG, the damping of oscillation mode corresponding to $\lambda_9$ and $\lambda_{10}$ declines when $Z_l$ increases. Unstable subsynchronous oscillation will appear in ROCOF-droop IG system when $Z_l$ exceeds 0.3 p.u.. The above results imply that it may destabilize the whole system by connecting ROCOF-droop IG to weak power grid and VSG control is suggested to be applied in IGs connected in a weak grid.

#### 2) Impact of Voltage Level on Stability

As the ratio of grid resistance $R_l$ and inductance $L_l$ of AC system in Fig. 1, $r_{R/X}$ is defined by (11).

$$r_{R/X} = R_l / \left(100\pi L_l\right) \tag{11}$$

The value of $r_{R/X}$ can reflect the voltage level of AC system because a smaller $r_{R/X}$ will accordingly appear in a higher voltage power grid. Corresponding to voltage levels of 10 kV and 500 kV, the typical values of $r_{R/X}$ are 6 and 0.1, respectively. For studying the system stability at most kinds of voltage levels, the eigenvalue trajectories when sweeping $r_{R/X}$ from 0.1 to 6 are shown in Fig. 10.

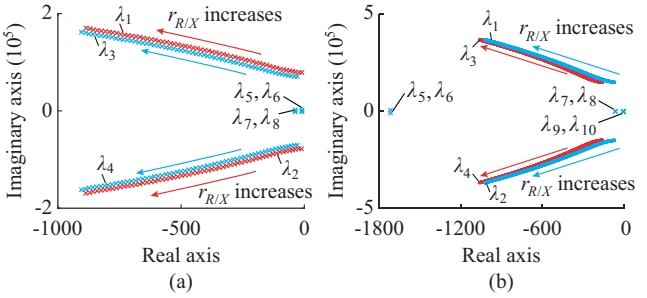


Fig. 10. Impact of $r_{R/X}$ on eigenvalues.

From Fig. 10, it is observed that $\lambda_1$-$\lambda_4$ monotonously move toward left in both IGs when $r_{R/X}$ increases. The other eigenvalues are insensitive to the change of $r_{R/X}$. For both control methods, no matter how $r_{R/X}$ changes, no right-half-plane pole is observed. Therefore, the instability caused by connecting IGs to grid with different voltage levels is not an important problem for choosing VSG control or ROCOF-droop control.

### D. Impact of PLL on Stability

The stability of ROCOF-droop IG is influenced by PLL. The eigenvalue trajectories of ROCOF-droop IG when sweeping the proportion coefficients of PLL ($K_{Ppll}$) from 1 to 100 are shown in Fig. 11.

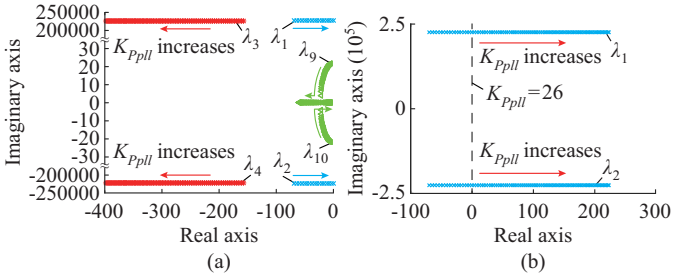


Fig. 11. Impact of $K_{Ppll}$ on eigenvalues. (a) Impact of $K_{Ppll}$ on $\lambda_1$-$\lambda_{10}$. (b) Impact of $K_{Ppll}$ on $\lambda_1$ and $\lambda_2$.

As shown in Fig. 11(a), $\lambda_1$ and $\lambda_2$ move toward right as $K_{Ppll}$

increases, which indicates that the corresponding damping ratio decreases. In contrast, the damping ratio of oscillation modes corresponding to $\lambda_3$, $\lambda_4$ and $\lambda_9$, $\lambda_{10}$ increases. The other eigenvalues are insensitive to the change of $K_{Ppll}$. Figure 11(b) shows that unstable high-frequency oscillation will appear in VSG system when $K_{Ppll}$ exceeds 26. However, no such stability problem will occur in VSG IG because PLL is not needed in it.

## V. Experimental Results

To validate the results obtained by eigenvalue analysis, the VSG IG and ROCOF-droop IG controllers are fabricated and tested on the RT-LAB semi-physical platform, as shown in Fig. 12, where FPGA stands for field programmable gate array. The key parameters of the test system are the same as those of the small-signal model, which are listed in Table I. The eigenvalue results from Figs. 7-11 indicate that VSG IG or ROCOF-droop IG will lose stabilization when $K_f$, $T_j$, $Z_l$ or $K_{Ppll}$ is set to be unsuitable. Table V gives the stability results obtained by eigenvalue analysis. Based on the cases given by Table V, the simulation results of RT-LAB semi-physical platform are shown by Fig. 13.

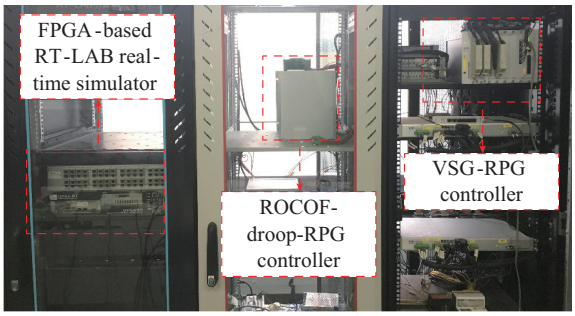


Fig. 12. RT-LAB semi-physical platform.

TABLE V
Results of Eigenvalue Analysis

| Case | Category of IG | Parameter | Change extent | Stability | Oscillation frequency (Hz) |
|---|---|---|---|---|---|
| 1 | VSG | $K_f$ | 8→6 | Unstable | 8.2 |
| 2 | VSG | $T_j$ | 8 s→10 s | Unstable | 7.8 |
| 3 | ROCOF-droop | $T_j$ | 0.01 s→1 s | Unstable | 3425.0 |
| 4 | ROCOF-droop | $Z_l$ | 0.06 p.u.→ 0.6 p.u. | Unstable | 2.5 |
| 5 | ROCOF-droop | $K_{Ppll}$ | 10→30 | Unstable | 3425.0 |

The results of Fig. 13(a) illustrate that VSG IG remains stable when $K_f$ equals to 8 but starts to vibrate when $K_f$ decreases to 6. This phenomenon is coinciding with the result of case 1 in Table V. The results of Fig. 13(a)-(e), which are obtained by RT-LAB test system, are respectively coinciding with the results of five modes in Table IV. This coincidence demonstrates the effectiveness of eigenvalue analysis, which proves the effectiveness of eigenvalue analysis.

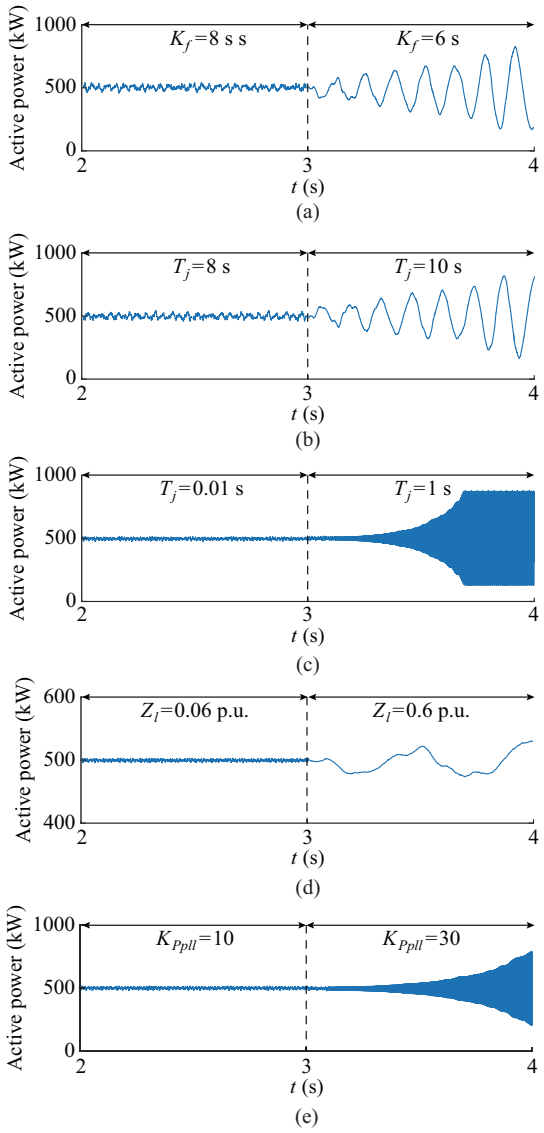


Fig. 13. Simulation results of RT-LAB semi-physical platform. (a) Case 1: VSG IG loses stability if $K_f$ decreases. (b) Case 2: VSG IG loses stability if $T_j$ increases. (c) Case 3: ROCOF-droop IG loses stability if $T_j$ increases. (d) Case 4: ROCOF-droop IG loses stability if $Z_l$ increases. (e) Case 5: ROCOF-droop IG loses stability if $K_{Ppll}$ increases.

## VI. Conclusion

This paper compares two categories of virtual inertia control for IGs, which are VSG control and ROCOF-droop control, from three perspectives: mathematical model, output characteristic and small-signal stability. The following conclusions can be drawn:

1) In VSG control, the swing equation of SGs is introduced in IGs to replace the original grid-connected current control to achieve inertial response, which makes IGs inherit stability problem of rotor angle from SGs. Meanwhile, ROCOF-droop control equips IGs with inertial response without the introduction of stability problem of rotor angle. However, in ROCOF-droop IG, derivative controller is applied in PLL to capture the ROCOF for emulating inertia, which will amplify high-frequency noise and may stimulate high-frequency vibration.

2) The principle of VSG IG to pick up the share of power impact is the same as that of SGs, which indicates that VSG IG inherits the response characteristic of transient active power output of SG. However, in the period from the impact load occurs until the governor action begins, ROCOF-droop IG cannot imitate the characteristics of active power output of SG.

3) The oscillation modal analysis clarifies that, because of the emulation of the swing equation, new oscillation modes which do not exist in the traditional IG are introduced by the application of VSG control. While the application of ROCOF-droop control equips IGs with inertial response without introduction of new oscillation mode. The results of eigenvalue trajectory imply that it may destabilize the whole system by connecting ROCOF-droop IG to weak power grid and VSG control is suggested to be applied in IGs connected in a weak grid.

## APPENDIX A

The state-space models of VSG IG and ROCOF-droop IG, which are given by (8) and (9), are rewrote in detailed by (A1) and (A2). The initial operation points of the states are denoted by subscript 0.

$$\begin{bmatrix} \frac{\mathrm{d}\Delta i_{id}}{\mathrm{d}t} & \frac{\mathrm{d}\Delta i_{iq}}{\mathrm{d}t} & \frac{\mathrm{d}\Delta u_{od}}{\mathrm{d}t} & \frac{\mathrm{d}\Delta u_{oq}}{\mathrm{d}t} & \frac{\mathrm{d}\Delta i_{od}}{\mathrm{d}t} & \frac{\mathrm{d}\Delta i_{oq}}{\mathrm{d}t} & \frac{\mathrm{d}\Delta\omega}{\mathrm{d}t} & \frac{\mathrm{d}\Delta\theta}{\mathrm{d}t} \end{bmatrix}^{\mathrm{T}} = \begin{bmatrix} \frac{-K_{P1}}{L_g} & 0 & -\frac{1}{L_g} & 0 & 0 & 0 & i_{iq0} & 0 \\ 0 & \frac{-K_{P1}}{L_g} & 0 & -\frac{1}{L_g} & 0 & 0 & i_{id0} & 0 \\ \frac{1}{C_g} & 0 & -\frac{1}{C_g} & 0 & 0 & \omega_g & u_{oq0} & 0 \\ 0 & \frac{1}{C_g} & 0 & \frac{1}{C_g} & -\omega_g & 0 & -u_{od0} & 0 \\ 0 & 0 & \frac{1}{L_g} & 0 & -\frac{R_1}{L_1} & \omega_g & i_{oq0} & \sin\left(\theta_0 u_{gd0}\right) \\ 0 & 0 & 0 & \frac{1}{L_g} & -\omega_g & -\frac{R_1}{L_1} & -i_{od0} & \cos\left(\theta_0 u_{gd0}\right) \\ 0 & 0 & 0 & 0 & 0 & 0 & \frac{K_f}{T_j} & 0 \\ 0 & 0 & 0 & 0 & 0 & 0 & 1 & 0 \end{bmatrix} \begin{bmatrix} \Delta i_{id} \\ \Delta i_{iq} \\ \Delta u_{od} \\ \Delta u_{oq} \\ \Delta i_{od} \\ \Delta i_{oq} \\ \Delta\omega \\ \Delta\theta \end{bmatrix} \tag{A1}$$

$$\begin{bmatrix} \frac{\mathrm{d}\Delta i_{id}}{\mathrm{d}t} \\ \frac{\mathrm{d}\Delta i_{iq}}{\mathrm{d}t} \\ \frac{\mathrm{d}\Delta u_{od}}{\mathrm{d}t} \\ \frac{\mathrm{d}\Delta u_{oq}}{\mathrm{d}t} \\ \frac{\mathrm{d}\Delta i_{od}}{\mathrm{d}t} \\ \frac{\mathrm{d}\Delta i_{oq}}{\mathrm{d}t} \\ \frac{\mathrm{d}\Delta x_{pll}}{\mathrm{d}t} \\ \frac{\mathrm{d}\Delta\theta_{pll}}{\mathrm{d}t} \\ \frac{\mathrm{d}\Delta u_{vd}}{\mathrm{d}t} \\ \frac{\mathrm{d}\Delta u_{vq}}{\mathrm{d}t} \end{bmatrix} = \begin{bmatrix} 0 & \omega_g & -\frac{1}{L_g} & 0 & 0 & 0 & 0 & 0 & 0 & 0 \\ -\omega_g & 0 & 0 & -\frac{1}{L_g} & 0 & 0 & 0 & 0 & 0 & 0 \\ \frac{1}{C_g} & 0 & -\frac{1}{C_g} & 0 & 0 & \omega_g & 0 & 0 & 0 & 0 \\ 0 & \frac{1}{C_g} & 0 & -\frac{1}{C_g} & -\omega_g & 0 & 0 & 0 & 0 & 0 \\ 0 & 0 & \frac{1}{L_1} & 0 & -\frac{R_1}{L_1} & \omega_g & 0 & \frac{\sin\left(\theta_{pll0}\right)u_{gd0}}{L_1} & 0 & 0 \\ 0 & 0 & 0 & \frac{1}{L_1} & -\omega_g & -\frac{R_1}{L_1} & 0 & \frac{\cos\left(\theta_{pll0}\right)u_{gd0}}{L_1} & 0 & 0 \\ 0 & 0 & 0 & -\frac{K_{Ipll}}{V_b} & 0 & 0 & 0 & 0 & 0 & 0 \\ 0 & 0 & 0 & \frac{K_{Ppll}}{V_b} & 0 & 0 & -1 & 0 & 0 & 0 \\ -K_{I1} & 0 & 0 & 0 & 0 & 0 & -\frac{K_{I1}K_f}{f_0} & \frac{K_{I1}T_j}{f_0} & 0 & 0 \\ 0 & -K_{I2} & 0 & 0 & 0 & 0 & 0 & 0 & 0 & 0 \end{bmatrix} \begin{bmatrix} \Delta i_{id} \\ \Delta i_{iq} \\ \Delta u_{od} \\ \Delta u_{oq} \\ \Delta i_{od} \\ \Delta i_{oq} \\ \Delta x_{pll} \\ \Delta\theta_{pll} \\ \Delta u_{vd} \\ \Delta u_{vq} \end{bmatrix} \tag{A2}$$

## REFERENCES


[1] Q. Zhong and T. Hornik, *Control of Power Inverters in Renewable Energy and Smart Grid Integration*. New York: Wiley-IEEE Press, 2013.

[2] Z. Lv, W. Sheng, Q. Zhong *et al*., "Virtual synchronous generator and its applications in micro-grid," *Proceedings of the CSEE*, vol. 34, no. 16, pp. 2591-2603, Jun. 2014.

[3] D. Sun, X. Xie, J. Wang *et al*., "Integrated generation-transmission expansion planning for offshore oilfield power systems based on genetic Tabu hybrid algorithm," *Journal of Modern Power Systems and Clean Energy*, vol. 5, no. 1, pp. 117-125, Jan. 2017.

[4] K. Sakimoto, Y. Miura, and T. Ise, "Stabilization of a power system including inverter-type distributed generators by a virtual synchronous generator," *Electrical Engineering in Japan*, vol. 187, no. 3, pp. 7-17, May 2014.

[5] H. P. Beck and R. Hesse, "Virtual synchronous machine," in *Proceeding of 9th International Conference on Electrical Power Quality and Utilization*, Barcelona, Spain, Oct. 2007, pp. 1-6.

[6] H. Li, X. Zhang, Y. Wang *et al*., "Virtual inertia control of DFIG-based wind turbines based on the optimal power tracking," *Proceedings of the CSEE*, vol. 32, no. 7, pp. 32-39, Mar. 2012.

[7] T. V. Van, K. Visscher, J. Diaz *et al*., "Virtual synchronous generator: an element of future grid," in *Proceedings of IEEE Innovative Smart Grid Technologies Conference Europe*, Gothenburg, Sweden, Oct.

2010, pp. 1-7.
[8] Q. -C. Zhong and G. Weiss, "Synchronverters: inverters that mimic synchronous generators," *IEEE Transactions on Industrial Electronics*, vol. 58, no. 4, pp. 1259-1267, Apr. 2011
[9] Q. Zhong, P. Nguyen, Z. Ma *et al*., "Self-synchronized synchronverters: inverters without a dedicated synchronization unit," *IEEE Transactions on Power Electronics*, vol. 29, no. 2, pp. 617-630, Feb. 2014.
[10] T. Zheng, L. Chen, T. Chen *et al*., "Review and prospect of virtual synchronous generator technologies," *Automation of Electric Power Systems*, vol. 39, no. 21, pp. 165-175, Nov. 2015.
[11] Y. Zhao, J. Chai, S. Wang *et al*., "Instantaneous power calculation based on intrinsic frequency of single-phase virtual synchronous generator," *Journal of Modern Power Systems and Clean Energy*, vol. 5, no. 5, pp. 1-9, Sept. 2017.
[12] M. Guan, W. Pan, Q. Zhang *et al*., "Synchronous generator emulation control strategy for voltage source converter (VSC) stations," *IEEE Transactions on Power Systems*, vol. 30, no. 6, pp. 3093-3101, Nov. 2015.
[13] T. Zheng, L. Chen, Y. Guo *et al*., "Flexible unbalanced control with peak current limitation for virtual synchronous generator under voltage sags," *Journal of Modern Power Systems and Clean Energy*, vol. 6, no. 1, pp. 61-72, Jan. 2018.
[14] J. Ge, H. Liu, H. Jiang *et al*., "Analysis and investigation on grid connected operation adaptability of virtual synchronous generator," *Automatic of Electric Power System*s, vol. 42, no. 9, pp. 26-35, May 2018.
[15] D. Sun, X. Xie, Y. Liu *et al*., "Investigation of SSTI between practical MMC-based VSC-HVDC and adjacent turbogenerators through modal signal injection test," *IEEE Transactions on Power Delivery*, vol. 32, no. 6, pp. 2432-2441, Dec. 2017.
[16] J. Jia, G. Yang, A. Nielsen *et al*., "Impact of VSC control strategies and incorporation of synchronous condensers on distance protection under unbalanced faults," *IEEE Transactions on Industrial Electronics*, vol. 66, no. 2, pp. 1108-1118, Feb. 2019.
[17] T. Shintai, Y. Miura, T. Ise *et al*., "Oscillation damping of a distributed generator using a virtual synchronous generator," *IEEE Transactions on Power Delivery*, vol. 29, no. 2, pp. 668-676, Apr. 2014.
[18] R. Shi, X. Zhang, C. Hu *et al*., "Self-tuning virtual synchronous generator control for improving frequency stability in autonomous photovoltaic-diesel microgrids," *Journal of Modern Power Systems and Clean Energy*, vol. 6, no. 3, pp. 482-494, May 2018.
[19] N. Ullah, T. Thiringer, and D. Karlsson, "Temporary primary frequency control support by variable speed wind turbines – potential and applications," *IEEE Transactions on Power Systems*, vol. 23, no. 2, pp. 601-612, May 2008.
[20] X. Qin, L. Su, Y. Chi *et al*., "Functional orientation discrimination of inertia support and primary frequency regulation of virtual synchronous generator in large power grid," *Automation of Electric Power Systems*, vol. 42, no. 9, pp. 36-43, May 2018.
[21] J. Liu, Y. Miura, and T. Ise, "Comparison of dynamic characteristics between virtual synchronous generator and droop control in inverter-based distributed generators," *IEEE Transactions on Power Electronics*, vol. 31, no. 5, pp. 3600-3611, May 2016.
[22] D. Sun, H. Liu, S. Gao *et al*., "Small-signal stability modeling and stability analysis of current-controlled virtual synchronous generators," *Power System Technology*, vol. 42, no. 9, pp. 2983-2991, Sept. 2018.
[23] P. Anderson, *Power System Control and Stability*. Ames: Iowa State University Press, 1977.

**Dawei Sun** is an engineer of State Grid Jibei Electric Power Research Institute, Beijing, China. His research interests include renewable power stability and VSC-HVDC transmission systems.

**Hui Liu** is a professorate senior engineer of State Grid Jibei Electric Power Research Institute, Beijing, China. His research interests include renewable power system, subsynchronous resonance evaluation and its countermeasures, power system analysis, VSC-HVDC and flexible AC transmission systems.

**Shunan Gao** is a senior engineer of State Grid Jibei Electric Power Research Institute, Beijing, China. His research interests include power system stability and renewable power plant control system.

**Linlin Wu** is a senior engineer of State Grid Jibei Electric Power Research Institute, Beijing, China. His research interests include wind generator control system and renewable power plant control system.

**Peng Song** is a senior engineer of State Grid Jibei Electric Power Research Institute, Beijing, China. His research interests include wind generator control system and renewable power plant control system.

**Xiaosheng Wang** is an engineer of State Grid Jibei Electric Power Research Institute, Beijing, China. His research interests include wind generator control system and grid-connected inverter controller.